ACS Catalysis

pubs.acs.org/acscatalysis

Research Article

Electrosynthesis of Ammonia Using Porous Bimetallic Pd−Ag Nanocatalysts in Liquid- and Gas-Phase Systems

Mohammadreza Nazemi, Pengfei Ou, Abdulaziz Alabbady, Luke Soule, Alan Liu, Jun Song, Todd A. Sulchek, Meilin Liu, and Mostafa A. El-Sayed*

Cite This: *ACS Catal.* 2020, 10, 10197−10206

Read Online

ACCESS | Metrics & More | Article Recommendations | Supporting Information

ABSTRACT: Cost-effective production of ammonia via electrochemical nitrogen reduction reaction (NRR) hinges on N_2 electrolysis at high current densities with suitable selectivity and activity. Here, we report our findings in electrochemical NRR for ammonia synthesis using porous bimetallic Pd−Ag nanocatalysts in both gas-phase and liquid-phase electrochemical cells at current densities above 1 mA cm^{-2} under ambient conditions. While the gas-phase cell has lower Ohmic losses and higher energy efficiency, the liquid-phase cell achieved higher selectivity and Faradaic efficiency, attributed to the presence of concentrated N_2 molecules dissolved in an aqueous electrolyte and the hydration effects. The liquid cell demonstrated notable performance for electrocatalytic NRR, achieving an NH_3 production rate of 45.6 ± 3.7 $\mu g\ cm^{-2}\ h^{-1}$ at a cell voltage of −0.6 V (vs RHE) and current density of 1.1 mA cm^{-2}, corresponding to a Faradaic efficiency of ∼19.6% and an energy efficiency of ∼9.9%. Similarly, the gas-phase cell achieved a NH_3 yield rate of 19.4 ± 2.1 $\mu g\ cm^{-2}\ h^{-1}$ at −0.07 V (vs RHE) and 1.15 mA cm^{-2} with a Faradaic efficiency of 7.9% and an energy efficiency of 27.1%. Further, *operando* surface-enhanced Raman spectroscopy and density functional theory (DFT) are used to identify intermediate species relevant to the NRR at the electrode−electrolyte interfaces to provide insights into the NRR mechanism on Pd−Ag nanoparticles. This work highlights the importance of design and optimization of cell configuration in addition to the modification of the catalyst to achieve high-performance N_2 electrolysis for ammonia synthesis.

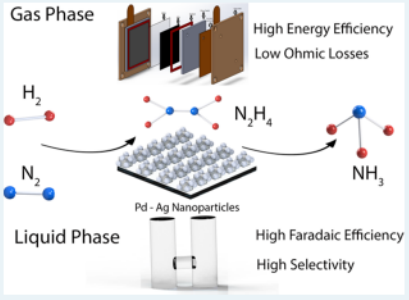

KEYWORDS: *ammonia electrosynthesis, nanoporous structures, electrolysis, SERS, DFT calculation*

INTRODUCTION

Satisfying global energy needs in an environmentally friendly manner is a great challenge that we face today and has become increasingly urgent. Fossil fuels such as oil, gas, and coal currently meet 80% of the global energy demand, resulting in the emission of 35 billion metric tons of carbon dioxide (CO_2) annually.[1] To mitigate the emission of CO_2, a promising solution is to extract energy from renewable energy sources such as solar and wind. Unfortunately, however, the renewable energy sources are either intermittent in nature or remote in location; there is a need to develop cost-effective and sustainable methods of storing this energy on an industrial scale when supply exceeds demand in the grid. As the cost of renewably derived electricity continues to decrease, one promising technique is the electrosynthesis of fuels and value-added chemicals.[2,3] Electrosynthesis enables the use of renewable electricity to convert low energy molecules (N_2) to high value-added molecules (NH_3) that can be utilized as either fuel, energy storage molecules, or chemicals.

Ammonia is a critical agrochemical and an essential precursor for pharmaceutical and industrial products.[4−6] Ammonia is also an attractive carbon-neutral liquid fuel to store intermittent renewable energy sources when supply exceeds demand in the grid as well as for power generation because of the compound high energy density (5.6 MW h ton^{-1}) and hydrogen content (17.6 wt %).[7] Electrochemical nitrogen reduction reaction (NRR) for ammonia synthesis might offer an alternative means to the capital- and carbon-intensive thermochemical process (Haber−Bosch) in a clean, sustainable, and decentralized way if the process is coupled to renewable electricity sources. In this scenario, an integrated system by coupling a photovoltaic (PV) cell to an electrochemical cell or a single photoelectrochemical device can be developed for solar-fuel based applications.[8−12] One of the challenges in electrochemical ammonia synthesis is finding catalysts that have a suitable activity for breaking the N_2 triple bond in aqueous media under ambient conditions.[13−16] Improving the design of electrocatalysts, electrolytes, and electrochemical cells is required to overcome the selectivity and activity barrier in electrochemical NRR.[17,18]

Received: June 17, 2020
Revised: July 13, 2020
Published: August 13, 2020

https://dx.doi.org/10.1021/acscatal.0c02680
ACS Catal. 2020, 10, 10197−10206

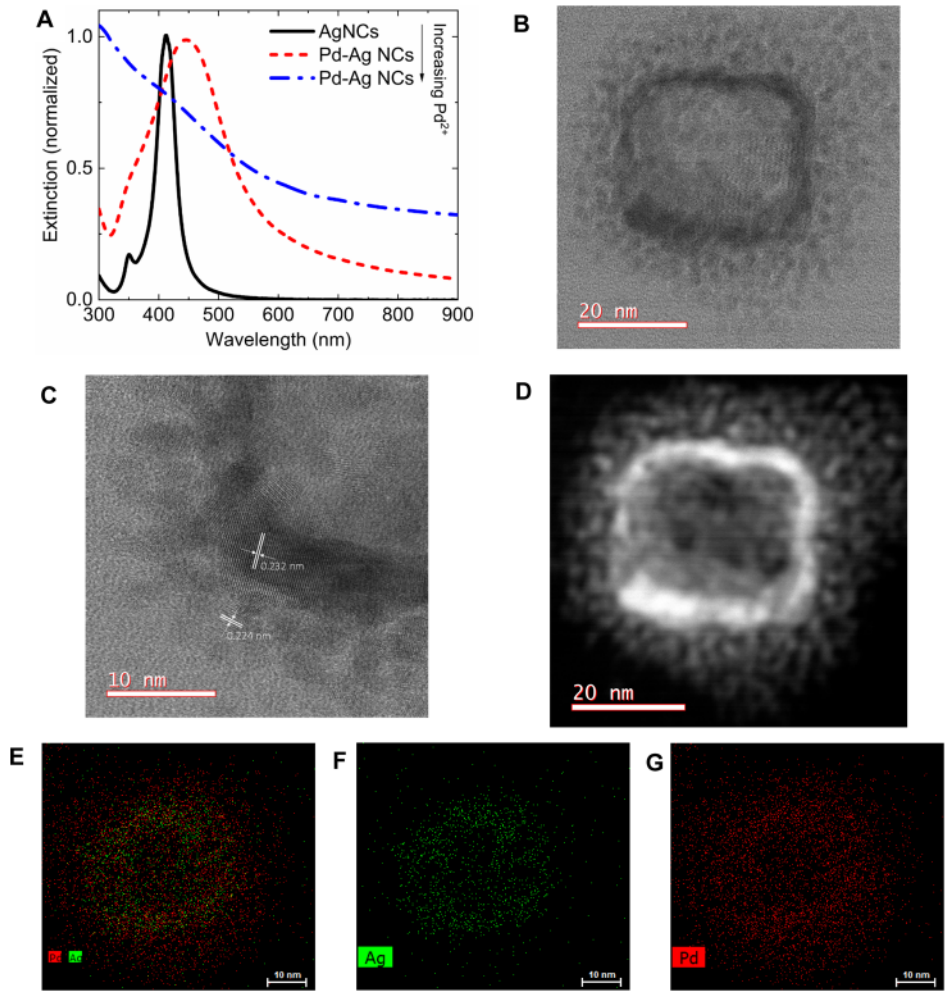

Figure 1. (A) UV−Vis extinction spectra of silver nanocubes and bimetallic Pd−Ag nanocages with various amount of Pd salt added. The LSPR peak of AgNCs shifts to red and becomes broader as the amount of Pd salt increases. TEM images of (B) Bimetallic Pd−Ag nanocages, (C) HRTEM image of Pd−Ag nanocages, (D) STEM and EDX elemental mapping (E−G) of a representative single bimetallic Pd−Ag nanoparticle. Silver nanocubes with the LSPR peak position at 412 nm are used as a template to synthesize various bimetallic nanoparticles.

Previous studies on the electrochemical NRR have focused on designing new electrocatalysts at low operating current densities (typically <200 μA cm^{-2}) with an enhanced N_2 selectivity in aqueous solutions or ionic liquids.[19−28] While nonaqueous solvents have been shown to suppress the hydrogen evolution reaction (HER) and to enhance the NRR Faradaic efficiency, they suffer from poor electrolyte conductivity and low energy efficiency.[29−31] To realize the commercialization of the electrochemical NRR process, N_2 electrolysis must be achieved at high current densities with high selectivity and activity. In addition to the design and optimization of electrocatalysts and electrolytes, another path to developing commercial NRR processes is designing electrochemical cells with low Ohmic resistance. This translates to the facilitation of reactant interactions with the electrode surface. The fuel cell-type electrochemical cell that consists of a membrane-electrode assembly (MEA) and gas diffusion layers (GDLs) has been shown to enable gas-phase NH_3 synthesis from N_2 and H_2.[32,33] It has been demonstrated that the kinetics of the rate-determining step in NRR (N_2* → N_2H*) is accelerated on transition-metal hydrides, where H* species on the catalyst surface directly react with the dissolved nitrogen in the electrolyte to form N_2H*.[34−36] Recently, it was shown that electrochemical NRR takes place on the surface of the Pd catalyst through the formation of Pd hydrides (PdH_x) at low overpotentials, followed by surface hydrogenation reactions.[36] The formation of PdH_x decreases the proton (H^+) adsorption strength on the Pd surface. It was found that the presence of Li^+ cations in the electrolyte enhances the electrochemical NRR because of the strong interaction of Li^+-N_2 and the ability of Li^+ to suppress the HER process by limiting the access of water molecules to the electrode surface.[37−39]

Here, we demonstrate the N_2 electrolysis for ammonia synthesis using porous bimetallic Pd−Ag nanoparticles as an electrocatalyst in both a fuel cell-type electrochemical cell (gas-phase) and H-cell (liquid-phase) at current densities above 1 mA cm^{-2} under ambient conditions. Reactants in the liquid-phase are N_2 and H_2O in a 0.5 M $LiClO_4$ (aq.) electrolyte, and gaseous N_2 and H_2 are reacted at the cathode and anode in the gas-phase system. A previous study found that increasing the Pd content (up to a Pd content of 57.7% at.) in porous trimetallic Au−Ag−Pd nanoparticles increases the electrocatalytic NRR activity.[23] Here, we aim to synthesize porous bimetallic Pd−Ag nanoparticles that allow the Pd content to be increased to 80%, while maintaining the porosity of the nanostructure. The electronic structure of the nanoparticles is explored by measuring the position of the d-band center of

https://dx.doi.org/10.1021/acscatal.0c02680
ACS Catal. 2020, 10, 10197−10206

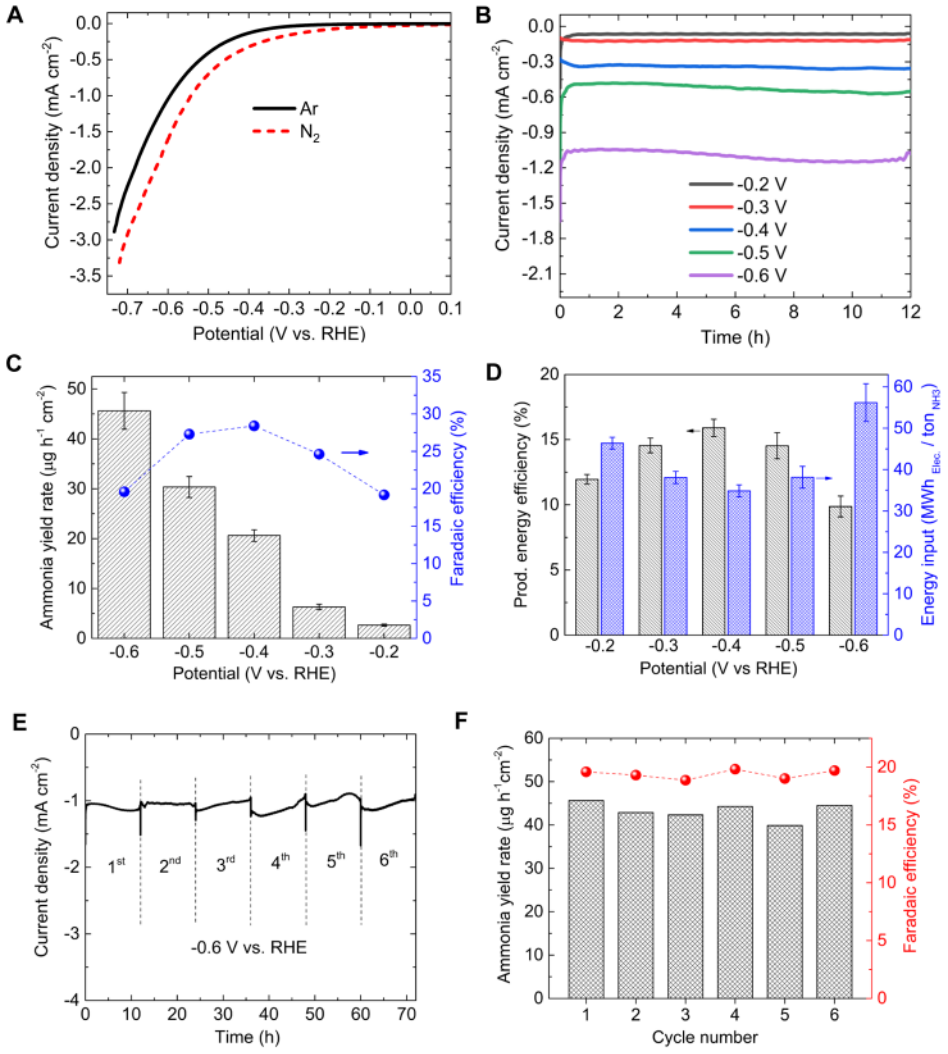

Figure 2. (A) LSV tests of Pd−Ag nanoparticles in an Ar- and N_2-saturated 0.5 M $LiClO_4$ (aq.) under ambient conditions with a scan rate of 10 mV s^{-1}. (B) CA results of Pd−Ag nanoparticles at a series of applied potentials. (C) Ammonia yield rate and Faradaic efficiency at various applied potentials in 0.5 M $LiClO_4$ (aq.) solution using Pd−Ag nanoparticles. (D) Production energy efficiency and energy input at various applied potentials using Pd−Ag nanoparticles. (E) CA tests for the stability of Pd−Ag nanoparticles at −0.6 V vs RHE in a 0.5 M $LiClO_4$ (aq.) solution. For each cycle, a CA test was carried out at −0.6 V vs RHE for 12 h. (F) Cycling stability results of the ammonia yield rate and FE on Pd−Ag nanoparticles.

nanoparticles and further understanding the binding strength of N-containing adsorbates with the catalyst surface. Transport phenomena in the electrochemical NRR at the solid−liquid interface are investigated using a rotating disk electrode (RDE) setup. We perform *operando* surface-enhanced Raman spectroscopy (SERS) and density functional theory (DFT) calculations to identify the species relevant to electrochemical NRR at the electrode−electrolyte interface and to gain an insight into the NRR mechanism.

RESULTS AND DISCUSSION

Porous bimetallic Pd−Ag nanoparticles are synthesized by adding K_2PdCl_4 (aq.) solution to solid silver nanocubes (AgNCs) dispersed in DI water that have a localized surface plasmon resonance (LSPR) peak position at 412 nm (Figure 1A,B).[40] As the amount of the Pd^{2+} precursor increases, the LSPR peak position redshifts, and the peak bandwidth increases (Figure 1A). PdNCs show only a background spectrum formed by d-to-d electron transitions (an interband transition spectrum) (Figure 1A). The redshift of the LSPR peak is because of the change in the shape of AgNCs as well as the change in the dielectric constant of the surrounding medium, resulting from the replacement of the Ag atoms in the AgNCs with Pd atoms (galvanic replacement) or the growth of Pd on Ag (Figure 1B). Because of the lattice mismatch between Pd (3.890 Å) and Ag (4.086 Å), when Pd^{2+} precursor is added to the solution of AgNCs, islands of palladium are formed on the Ag surface. Further addition of Pd salt solution causes the islands to grow and form a rough and porous surface layer (Figure 1C,D). High-resolution transmission electron microscopy (HRTEM) shows lattice spacings of 0.232 and 0.224 nm, which correspond to the (111) lattice plane of the face-centered cubic (FCC) structure Ag and Pd (Figure 1C).

Scanning transmission electron microscopy (STEM) and energy-dispersive X-ray (EDX) spectroscopy are performed to determine the structure, the elemental composition, and the distribution of Pd−Ag nanoparticles (Figure 1E−G). The reduction of Pd^{2+} to Pd^0 is accomplished through two different mechanisms. The galvanic replacement process ($Pd^{2+}_{(aq.)}$ + $2Ag_{(s)}^0 \rightarrow Pd_{(s)}^0 + 2Ag_{(aq.)}^+$) leads to the formation of a hollow

https://dx.doi.org/10.1021/acscatal.0c02680
ACS Catal. 2020, 10, 10197−10206

Pd−Ag nanostructure. The second mechanism is an island-growth mode that results in the creation of a continuous porous layer of Pd on Ag at the exterior surface (Figure 1E−G). The Pd and Ag contents of the bimetallic nanoparticles are provided in Table S1.

X-ray photoelectron spectroscopy (XPS) results of bimetallic nanoparticles reveal a spin−orbit doublet for Ag 3d at 367.9 and 373.9 eV, which is consistent with a prior study for trimetallic Au−Ag−Pd nanoparticles (Figure S1).[23] The Pd 3d spectrum is deconvoluted into two pairs of doublets. The doublet peaks at 336.0 and 341.3 eV correspond to metallic Pd, and the doublet peaks at higher binding energies and with lower intensities (337.6 and 343.0 eV) are attributed to oxidized Pd states (Pd^{n+}) (Figure S1). The Pd 3d peaks shift to higher binding energies (0.5 eV) compared to those of trimetallic Au−Ag−Pd nanoparticles, which might be attributed to the less charge distribution in the bimetallic compared to the trimetallic nanoparticles.[23]

The electrochemical surface area of Pd ($ECSA_{Pd}$) in the Pd−Ag nanoparticles is determined to be 277.5 $m^2\ g^{-1}$, which is approximately four times higher than that of commercial Pd/C catalysts (Figure S2, Table S1).[23] Linear sweep voltammetry (LSV) tests are performed in Ar- and N_2-saturated 0.5 M $LiClO_4$ (aq.) electrolyte in an H-type cell, where a proton exchange membrane separated the anodic and cathodic compartments (Figure 2A). A neutral pH electrolyte was selected in this study based on the optimization of the electrolyte pH to obtain the highest electrocatalytic NRR activity. In a wide potential window ($-0.7 < E < 0$), a higher current density at a given potential is achieved in the N_2-saturated electrolyte. At high negative potentials where HER becomes dominant, the N_2-saturated electrolyte has a higher current density than an Ar-saturated electrolyte, indicating that electrochemical NRR at higher current densities (in the order of milliamperes per centimeter squared) is feasible (Figure 2A).

Chronoamperometry (CA) tests are performed at a series of applied potentials using Pd−Ag nanoparticles to determine the ammonia yield rate and FE (Figure 2B,C). Each measurement was repeated three times and on different days, and the standard deviation was calculated based on three independent measurements to evaluate the reproducibility of the experimental results. As the potential becomes more negative, the ammonia yield rate increases, reaching a maximum at −0.6 V ($45.6 \pm 3.7\ \mu g\ cm^{-2}\ h^{-1}$), which corresponds to an FE of 19.6%. This activity outperforms NRR activities reported on prior studies using Pd-based nanoparticles (Table S2). The FE at −0.6 V was lower than other applied potentials because of the compromise between increasing current density and competitive selectivity toward HER rather than NRR. The work function (Φ) of Pd−Ag nanoparticles is 4.54 eV, which is measured via ultraviolet photoelectron spectroscopy (UPS) (Figure S3). The downshift in the d-band center ($E - E_f$) of Pd−Ag nanoparticles (−4.54 eV) compared to that of trimetallic Au−Ag−Pd nanoparticles (−3.73 eV) in the previous work resulted in lower selectivity of N-containing adsorbates on the catalyst surface and therefore lower FE for Pd−Ag nanoparticles compared to the trimetallic Au−Ag−Pd nanoparticles.[23] However, because of the enhanced $ECSA_{Pd}$ and higher Pd content (81.2% at.), higher current densities and ammonia yield rates were observed using Pd−Ag nanoparticles. A production energy efficiency of 9.9% is achieved at −0.6 V, which corresponds to an electrical energy input of 56.2 MW h per ton of ammonia (Figure 2D). Most input electrical energy (>70%) is consumed at the anode side, where the oxygen evolution reaction (OER) takes place, which is added to additional ohmic losses (e.g., electrode and electrolyte resistances) in the liquid-phase system. The OER has a high thermodynamic potential (1.23 V) and sluggish reaction kinetics that results in a total cell potential higher than 2.0 V with the oxygen gas as a product that may be discharged and wasted. A CA test is performed at −0.6 V for 72 h by conducting six consecutive cycles, each for 12 h, to evaluate the stability of Pd−Ag nanoparticles (Figure 2E). The electrocatalyst could maintain continuous NH_3 formation with an average NH_3 yield rate of 43.23 $\mu g\ cm^{-2}\ h^{-1}$ and FE of 19.4% (Figure 2F). The turnover frequency (TOF) is determined to be 147 h^{-1} as per active Pd and Ag sites (see Supporting Information for detailed calculations). SEM images before and after the stability test reveal that the nanoparticles are still anchored to the substrate and are not washed away in the long-term experiment under stirring and applied bias (Figure S4). TEM images after the stability test show minor morphology changes of the nanoparticles after 72 h of the CA test (Figure S5). A monolayer of nanoparticles on a Si substrate is prepared via the Langmuir−Blodgett technique to evaluate the mechanical stability of hollow nanoparticles (Figure S6). As hollow nanoparticles are more fragile than their solid counterparts and are susceptible to failure and collapse during catalysis, the stiffness of nanoparticles after the long-term stability test is measured via atomic force microscopy (AFM) (Figure S7). The stiffness of Pd−Ag nanoparticles is measured to be primarily within the range of 1−6 GPa, which is comparable to the stiffness of hollow Pd nanoparticles of similar size and structure in prior studies.[41,42] The role of the temperature on the electrocatalytic NRR activity is evaluated (Figure S8). By increasing the reaction temperature, the NRR activity increases, which is attributed to the faster mass transport rate of reactants at higher temperatures (Figure S9). The overall activation energy of the electrochemical NRR on Pd−Ag nanoparticles is determined to be 73.6 kJ mol^{-1} (Figure S10).

We performed similar experiments in a nonaqueous electrolyte [0.5 M $LiClO_4$ in tetrahydrofuran (THF) solution and ethanol (1% vol)] (Figures S11−S13). A low current density (~8 $\mu A\ cm^{-2}$) is achieved at a high applied potential (−3.0 V vs Ag/AgCl), resulting in energy efficiency lower than that of aqueous solution at a comparable FE (Figure S13). To improve the energy efficiency of the electrochemical NRR, a gas-phase electrochemical cell is used, consisting of an MEA and GDLs (Figure S14). By decreasing the distance between the cathode and anode and eliminating the liquid electrolyte, MEAs can reduce the Ohmic losses in the electrochemical cell.[43−45] Pure H_2 is fed into the anode, where the hydrogen oxidation reaction (HOR) ($H_2\ (g) \rightarrow 2H^+ + 2e^-$, $E_{RHE}^0 = 0$ V) occurs on the Pt-based nanoparticles (Figure S15). HER is a competing reaction with the NRR at the cathode; H_2 gas from this reaction can be recovered and fed to the anode. The HOR overpotential is lower than that of OER on the Pt-based catalysts.[46] CA tests are conducted at lower applied potentials than those of the liquid-phase system (Figure S16). The same catalytic activity trend as the liquid phase is observed in the gas phase but with a lower ammonia yield rate ($19.4 \pm 2.1\ \mu g\ cm^{-2}\ h^{-1}$) and FE (7.9%) at an applied potential of −0.07 V with a comparable current density (1.15 mA cm^{-2} @−0.07 V in the gas phase vs 1.1 mA cm^{-2} @−0.6 V in the liquid phase)

https://dx.doi.org/10.1021/acscatal.0c02680
ACS Catal. 2020, 10, 10197−10206

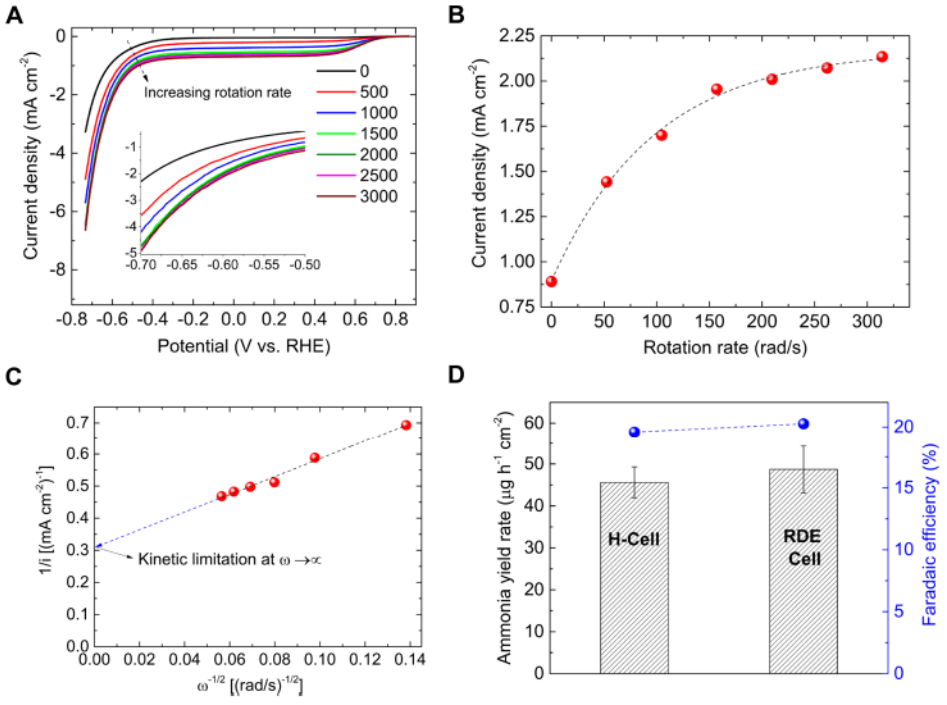

Figure 3. (A) LSV tests of Pd−Ag nanoparticles in an N_2-saturated 0.5 M $LiClO_4$ (aq.) solution in an RDE setup at various rotation rates (rpm) with a scan rate of 10 mV s^{-1}. (B) Current density at a potential of −0.6 V vs RHE for various rotation rates. At higher rotation rates, a marginal increase in the current density is observed. (C) Koutecky−Levich plot from electrochemical NRR data on Pd−Ag nanocatalysts. (D) Ammonia yield rate and Faradaic efficiency in an H-cell and RDE cell (2500 rpm) at −0.6 V vs RHE in 0.5 M $LiClO_4$ (aq.) solution.

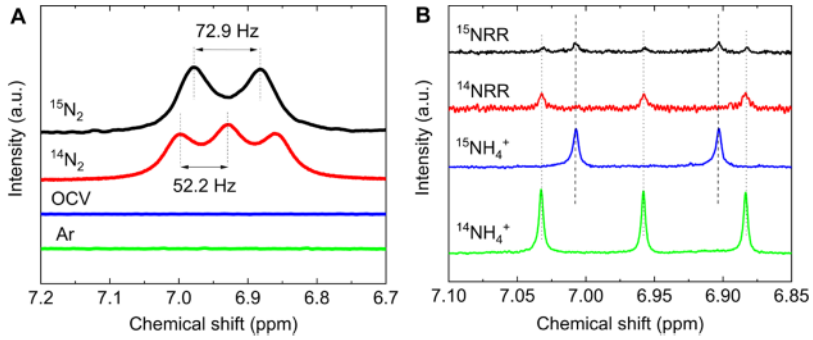

Figure 4. (A) ^1H NMR spectra of samples after electrochemical $^{15}N_2$ ($^{14}N_2$) reduction reaction at −0.6 V vs RHE using Pd−Ag nanoparticles in 0.5 M $LiClO_4$ (aq.) solution. The control experiments spectra (OCV and Ar) are also included, which reveal no distinct peaks associated to the ammonium. (B) ^1H NMR spectra of samples after electrochemical $^{15}N_2$ ($^{14}N_2$) reduction reaction at −3.0 V vs Ag/AgCl using Pd−Ag nanoparticles in nonaqueous electrolyte (0.5 M $LiClO_4$ in THF and 1% ethanol). Standard $^{15}NH_4^+$ and $^{14}NH_4^+$ samples (25 μM) were used for ammonia quantification in the nonaqueous solution.

(Figure S17). This performance corresponds to the energy efficiency of 27.1% and the energy input of 20.5 MW h per ton of ammonia, which is more efficient than the liquid phase because of lower Ohmic resistances (Figure S18). The highest energy efficiency achieved is 72.0% at an applied potential of −0.01 V, which is equivalent to an energy input of 7.7 MW h per ton of ammonia. This performance is achieved at a low current density of ∼0.17 ± 0.03 mA cm^{-2}, which is comparable with the state-of-the-art Haber−Bosch process that uses 7.8 MW h per ton of ammonia (based on the natural gas as an input feedstock).[7]

In order to fully understand the role of mass transport resistances at the electrode surface in the H-cell, rotating disk electrode (RDE) measurements are conducted with nanoparticles deposited on a glassy carbon electrode.[47] The overall current density on the RDE is related to the kinetic-limited (i_k) and diffusion-limited current density (i_d). The RDE data are analyzed using the Koutecky−Levich (K−L) equation which is given by

$$\frac{1}{i} = \frac{1}{i_k} + \frac{1}{i_d} \quad (1)$$

where i_d is proportional to the square root of rotation rate ($\omega^{1/2}$, rad/s). The LSV measurements are conducted at different rotation rates (0−3000 rpm) at a scan rate of 10 mV s^{-1} (Figure 3A). As the rotation rate increases, the value of the current density at −0.6 V vs RHE reaches a plateau, indicating that the reactant transport is no longer the limiting step (infinite mass transport) in the overall current density and the rate of the half-reaction would only be limited by the slow kinetics at an electrode surface (Figure 3B). This is also consistent with the CA data at various rotation rates, where at

https://dx.doi.org/10.1021/acscatal.0c02680
ACS Catal. 2020, 10, 10197−10206

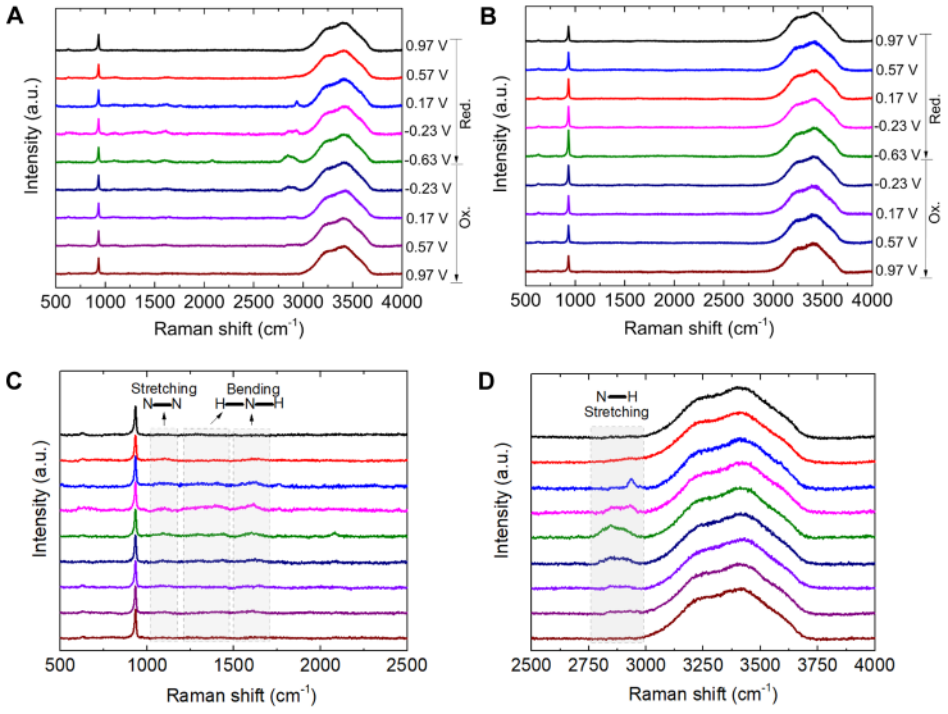

Figure 5. (A) *Operando* SERS using Pd−Ag nanoparticles in N_2-saturated 0.5 M $LiClO_4$ (aq.) solution at a scan rate of 2.5 mV s^{-1} with 532 nm laser. (B) *Operando* SERS using Pd−Ag nanoparticles in Ar-saturated 0.5 M $LiClO_4$ (aq.) solution at a scan rate of 2.5 mV s^{-1} with 532 nm laser. (C,D) Low and high Raman shift of SERS spectra in the N_2-saturated electrolyte (A).

the high rotation rate (i.e., 2500 rpm), the formation of bubbles at the electrode surface is limited because of the facile mass transport (Figure S19). The K−L plot reveals a linear relationship between $1/i$ and $\omega^{-1/2}$, highlighting the role of kinetic- and diffusion-limited current density on the overall current density at the electrode surface (Figure 3C). To understand the role of mass transport loss in the H-cell system, we performed electrochemical NRR with similar catalyst and reaction conditions (e.g., catalyst loadings, applied potential, etc.) in the H-cell system under vigorous stirring and in the RDE system without stirring at an electrode rotation rate of 2500 rpm. Comparable electrocatalytic NRR activity is observed in both setups, indicating that mass transport resistance in the H-cell will be sufficiently suppressed if the reactor is intensely stirred under reaction conditions (Figure 3D).

Control experiments are carried out in which Argon (Ar) and isotopically labeled N_2 are used as feed gases.[21,48−51] $^{15}N_2$ (98 atom % ^{15}N) was purified before use in experiments by passing through an absorber (1 mM H_2SO_4) followed by deionized water to remove any NO_x and NH_3 contamination. The amounts of ammonia are measured with Nessler's method and ^1H NMR (Figure S20). The calibration curves for ^1H NMR quantification are provided in our prior studies.[21,51] No ammonia is produced in experiments with similar operating conditions (e.g., catalyst type, loading) to those in Figure 2C but with Ar gas and N_2 gas at the open-circuit voltage (OCV) (Figure 4). Further, the doublet and triplet couplings of $^{15}N_2$ and $^{14}N_2$ with J-coupling constants of 72.9 and 52.2 Hz obtained from ^1H NMR measurement and the quantitative agreement between the amounts of ammonia produced using $^{14}N_2$ and $^{15}N_2$ confirm that the supplied N_2 is the major source of ammonia formation in the system (Figure 4A). The amounts of ammonia measured by ^1H NMR in ^{15}NRR and ^{14}NRR experiments are 706.7 μM for $^{15}N_2$ and 769.3 μM for $^{14}N_2$. These values are in close agreement with the amounts of ammonia measured by Nessler's method (804.9 ± 65.3 μM). The amounts of ammonia reported in this work are remarkably higher than the amount of ammonia that can be produced by even maximum contamination levels of various impurities (e.g., NO_x) that might be present in ultrahigh-purity (UHP) $^{14}N_2$ used for experiments. This also highlights the importance of operating N_2 electrolysis at high current densities to achieve high ammonia yield rates to rule out the false-positive results of ammonia formation by gas impurities.

The amounts of ammonia produced in the nonaqueous electrolyte were also comparable in the ^{14}NRR and ^{15}NRR (1.52 ± 0.37 μM) (Figure 4B). Some $^{14}NH_4^+$ is observed in the ^{15}NRR experiment, which is attributed to various sources of contamination in measurements.[48]

To probe possible reaction mechanisms and track the intermediate species relevant to NRR at the solid−liquid (electrode−electrolyte) interface, *operando* SERS spectra are collected during the CV tests in Ar- and N_2-saturated electrolytes on a SERS active substrate, which is comprised of Pd−Ag nanoparticles deposited on the Au thin film working electrode. During the positive scan (oxidation segment) of the CV test in the N_2-saturated electrolyte, a pronounced peak at ~0.6 V is observed, which is attributed to the oxidation of NH_3 (aq.) produced during NRR (Figure S21). The vibrational bands located at 933 and 3415 cm^{-1} in the SERS spectra in N_2- and Ar-saturated $LiClO_4$ (aq.) solutions are attributed to the stretching modes of the O−H and ClO_4^- anion (Figure 5A,B). Similar to the NRR mechanism on Au−Ag−Pd nanostructures in the previous study,[23] during the reductive pathway (0.97 to −0.23 V vs RHE), three small vibrational peaks at 1101, 1394 and 1613 cm^{-1} are observed, reaching their highest intensity at −0.23 V; these peaks can be classified as N−N stretching, H−

https://dx.doi.org/10.1021/acscatal.0c02680
ACS Catal. 2020, 10, 10197−10206

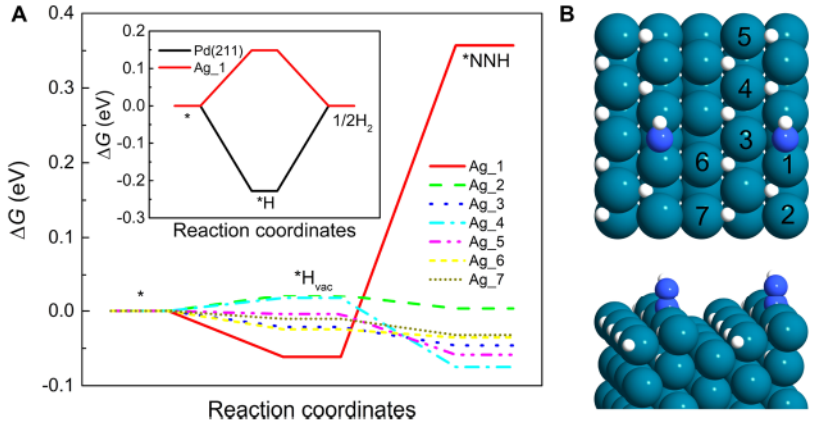

Figure 6. (A) Calculated free energy diagram for H vacancy formation ($*H_{vac}$) followed by $*N_2$ reduction to *NNH on the PdH (211) surface with Ag replacement at different sites. The free energies of $*H_{vac}$ and *NNH on the PdH (211) surface are used as the energy reference. The inset figure shows that the *H binding energy is weakened on the catalyst surface after replacing the Pd atom by the Ag atom at site 1. (B) Top and side views of the adsorbed *NNH on the PdH (211) surface. Ag_n denotes the different sites when Pd (n) is replaced by Ag.

N−H bending, and N−H wagging, indicating the formation of N_2H_4 as an intermediate species (Figure 5A, C).[52] A strong peak centered at 2936 cm^{-1} which appeared as a more negative potential (i.e., −0.63 V) is applied. This peak corresponds to the N−H asymmetric stretching mode. The evolution of this peak supports the formation of NH_4^+ during the reductive potential sweep.[52−54] The intensity of the peak for N−H stretching mode using Pd−Ag nanoparticles is significantly higher than that of Au−Ag−Pd nanoparticles, which is consistent with higher ammonia yield rates on Pd−Ag nanoparticles at lower FE. As the potential becomes more negative during the reductive CV scan (−0.23 to −0.63 V), the intensity of peaks at 1101, 1394, and 1613 cm^{-1} (intermediates) decreases, while the peak at 2936 cm^{-1} NH_4^+ reaches its highest intensity. This suggests the formation of NH_3 from the intermediate species ($N_2 \rightarrow N_2H_4 \rightarrow NH_3$) (Figure 5A,C,D). This also signifies the fact that no detectable amount of hydrazine (N_2H_4) is observed as a byproduct in electrochemical NRR studies using Pd-based nanocatalysts.[36,55,56] The intensity of the peaks ascribed to intermediates and ammonium decreases during the oxidative pathway because of the oxidation of the N-containing species, which is also consistent with the strong ammonium oxidation peak during the CV test (Figures 5C,D, S21). *Operando* SERS measurements in the Ar-saturated electrolyte with the electrocatalyst show no pronounced peaks, implying the peaks observed in the N_2-saturated electrolyte with the electrocatalyst are solely related to the formation of N-containing species at the presence of the electrocatalyst (Figure 5B).

To further understand the performance of Pd−Ag nanoparticles toward NRR, the free energy diagram of some key reaction intermediates [i.e., H vacancy ($*H_{vac}$) and *NNH] is examined using DFT calculations. For pristine Pd, it is known that the α-phase of PdH is the most thermodynamically stable phase under electrochemical operating conditions.[36] Thus, the model used for DFT calculations was a (211) surface of PdH, where 2/3 of the surface is covered by a monolayer of *H. The formation of H vacancies is required for N_2 to be adsorbed onto active edge sites of the Pd (211) surface. The thermodynamic energy barrier (ΔG) for $*H_{vac}$ formation is 0.12 eV, followed by an endothermic reaction step of $*N_2$ hydrogenation with a ΔG value of 1.24 eV. This step is the potential-determining step (PDS) (Figure S22). $*N_2$ hydrogenation is assisted by the Grotthuss-like proton-hopping mechanism present in a hydrated environment.[36]

The energy difference for Ag replacement at different sites in the structure is close in energy (Table S3). Therefore, seven different sites on the PdH (211) surface are examined to study the binding strength of adsorbates after replacing Pd atoms with Ag atoms. When Pd atoms closest to the adsorption sites (sites 1 and 2) are replaced by Ag, the binding energy of *NNH is weakened by 0.01 and 0.36 eV, respectively (Figure 6A,B). In addition, when Pd atoms far from the adsorption sites (sites 3−7) are replaced with Ag, the binding energies of *NNH for various adsorption sites are enhanced by ∼0.05 eV. Although replacing Pd by Ag on site 1 results in an increase in the thermodynamic energy barrier for $*N_2$ reduction to *NNH, it weakens the *H binding energy of Pd, raises the ΔG from −0.23 to 0.15 eV, thereby decreasing HER activity on the catalyst surface (Figure S23). Without the presence of Ag atoms, protons would cover most active sites on the Pd nanoparticles. Collectively, the presence of Ag in bimetallic Pd−Ag nanoparticles suppresses the HER and provides more intrinsically active sites for NRR. These calculations corroborate experimentally observed trends in NRR activity.

■ CONCLUSIONS

Electrochemical reduction of atmospheric nitrogen to ammonia in liquid- and gas-phase systems was demonstrated at current densities >1 mA cm^{-2} using porous bimetallic Pd−Ag nanoparticles. While a higher FE is achieved in the liquid phase (19.6%) compared to the gas phase (7.9%), the gas phase had a 2.7 × better energy efficiency (27.1%) because of a reduction in Ohmic losses. Mass transport resistance at the electrode surface was explored via RDE measurements. Vigorously stirring the reactor in the H-cell system suppressed mass transport losses, which was revealed by comparing the electrocatalytic NRR activity in the RDE setup and the H-cell system. *Operando* SERS showed that electrochemical NRR takes place on the Pd−Ag surface through an associative mechanism with N_2H_4 as an intermediate species. The appearance of the ammonia oxidation peak during CV measurements was consistent with the strong N−H stretching mode at 2936 cm^{-1}, which was attributed to the formation of ammonia during the reductive pathway.

https://dx.doi.org/10.1021/acscatal.0c02680
ACS Catal. 2020, 10, 10197−10206

This work highlights the importance of cell design and optimization in addition to the design of selective catalysts for high-performance N_2 electrolysis for ammonia synthesis. The work also used the combination of theory and *operando* measurements to understand the reaction mechanism to aid in designing more efficient catalysts for electrochemical energy conversion systems.

EXPERIMENTAL SECTION

Nanoparticle Synthesis. Porous bimetallic Pd−Ag nanoparticles are synthesized by adding K_2PdCl_4 (aq.) solution to a solid silver nanocube (AgNC) solution through the galvanic replacement method.[40] 5 mL of the cleaned AgNCs was diluted with 100 mL of DI water in a 150 mL round-bottomed flask. K_2PdCl_4 [0.006 M (aq.)] is gradually injected to the 100 mL AgNC solution (0.5 mL per 5 min) at room temperature (20 °C) under constant shaking until the LSPR of AgNC disappears [approximately 5 mL of K_2PdCl_4 (aq.) solution]. The resulting bimetallic Pd−Ag nanoparticles are washed twice by centrifugation at 12,000 rpm for 10 min. The precipitated nanoparticles are dispersed in DI water or ethanol for future use.

ASSOCIATED CONTENT

Supporting Information

The Supporting Information is available free of charge at https://pubs.acs.org/doi/10.1021/acscatal.0c02680.

Chemicals and materials, electrochemical measurement, working electrode preparation, instrumentation, FE and energy efficiency calculations, SEM and TEM images before and after the stability test, activation energy calculation, AFM measurement of nanoparticles, and CV measurement during *operando* SERS (PDF)

AUTHOR INFORMATION

Corresponding Author

Mostafa A. El-Sayed − *Laser Dynamics Laboratory, School of Chemistry and Biochemistry, Georgia Institute of Technology, Atlanta, Georgia 30332-0400, United States;* orcid.org/0000-0002-7674-8424; Email: melsayed@gatech.edu

Authors

Mohammadreza Nazemi − *Laser Dynamics Laboratory, School of Chemistry and Biochemistry and George W. Woodruff School of Mechanical Engineering, Georgia Institute of Technology, Atlanta, Georgia 30332-0400, United States;* orcid.org/0000-0002-1735-9277

Pengfei Ou − *Department of Mining and Materials Engineering, McGill University, Montreal, Quebec H3A 0C5, Canada;* orcid.org/0000-0002-3630-0385

Abdulaziz Alabbady − *School of Materials Science and Engineering, Georgia Institute of Technology, Atlanta, Georgia 30332-0405, United States*

Luke Soule − *School of Materials Science and Engineering, Georgia Institute of Technology, Atlanta, Georgia 30332-0405, United States*

Alan Liu − *George W. Woodruff School of Mechanical Engineering, Georgia Institute of Technology, Atlanta, Georgia 30332-0405, United States*

Jun Song − *Department of Mining and Materials Engineering, McGill University, Montreal, Quebec H3A 0C5, Canada;* orcid.org/0000-0003-3675-574X

Todd A. Sulchek − *George W. Woodruff School of Mechanical Engineering, Georgia Institute of Technology, Atlanta, Georgia 30332-0405, United States;* orcid.org/0000-0003-4196-6293

Meilin Liu − *School of Materials Science and Engineering, Georgia Institute of Technology, Atlanta, Georgia 30332-0405, United States;* orcid.org/0000-0002-6188-2372

Complete contact information is available at: https://pubs.acs.org/10.1021/acscatal.0c02680

Notes

The authors declare the following competing financial interest(s): M.N. and M.A.E. have filed a patent application for "Systems and Methods for Forming Nitrogen-Based Compounds" (U.S. Patent Application 16/788,656).

ACKNOWLEDGMENTS

This material is based upon work supported by the National Science Foundation under grant no. 1904351. This work was performed in part at the Georgia Tech Institute for Electronics and Nanotechnology, a member of the National Nanotechnology Coordinated Infrastructure (NNCI), which is supported by the National Science Foundation (grant ECCS-1542174). This work was partially supported by the Georgia Research Alliance based in Atlanta, Georgia.

REFERENCES

(1) Boden, T. A.; Marland, G.; Andres, R. J. *National CO2 Emissions from Fossil-Fuel Burning, Cement Manufacture, and Gas Flaring: 1751−2014*; Carbon Dioxide Information Analysis Center, Oak Ridge National Laboratory, US Department of Energy, 2017.

(2) De Luna, P.; Hahn, C.; Higgins, D.; Jaffer, S. A.; Jaramillo, T. F.; Sargent, E. H. What would it take for renewably powered electrosynthesis to displace petrochemical processes? *Science* **2019**, *364*, No. eaav3506.

(3) Yang, J.; Guo, Y.; Lu, W.; Jiang, R.; Wang, J. Emerging Applications of Plasmons in Driving CO2 Reduction and N2 Fixation. *Adv. Mater.* **2018**, *30*, 1802227.

(4) Smil, V. Detonator of the population explosion. *Nature* **1999**, *400*, 415.

(5) U.S. Geological Survey *Mineral Commodity Summaries 2016: US Geological Survey*; US Government Publishing Office: Washington, DC, 2016.

(6) U.S. Geological Survey *Mineral Commodity Summaries, 2009*; Government Printing Office: Washington, DC, 2009.

(7) Giddey, S.; Badwal, S. P. S.; Munnings, C.; Dolan, M. Ammonia as a renewable energy transportation media. *ACS Sustainable Chem. Eng.* **2017**, *5*, 10231−10239.

(8) Huan, T. N.; Dalla Corte, D. A.; Lamaison, S.; Karapinar, D.; Lutz, L.; Menguy, N.; Foldyna, M.; Turren-Cruz, S.-H.; Hagfeldt, A.; Bella, F.; Fontecave, M.; Mougel, V. Low-cost high-efficiency system for solar-driven conversion of CO2 to hydrocarbons. *Proc. Natl. Acad. Sci.* **2019**, *116*, 9735−9740.

(9) Gurudayal, G.; Bullock, J.; Srankó, D. F.; Towle, C. M.; Lum, Y.; Hettick, M.; Scott, M.; Javey, A.; Ager, J. Efficient solar-driven electrochemical CO_2 reduction to hydrocarbons and oxygenates. *Energy Environ. Sci.* **2017**, *10*, 2222−2230.

(10) Corby, S.; Francàs, L.; Kafizas, A.; Durrant, J. R. Determining the role of oxygen vacancies in the photoelectrocatalytic performance of WO3 for water oxidation. *Chem. Sci.* **2020**, *11*, 2907−2914.

(11) Ye, W.; Arif, M.; Fang, X.; Mushtaq, M. A.; Chen, X.; Yan, D. Efficient Photoelectrochemical Route for the Ambient Reduction of N2 to NH3 Based on Nanojunctions Assembled from MoS2 Nanosheets and TiO2. *ACS Appl. Mater. Interfaces* **2019**, *11*, 28809−28817.

(12) Schreier, M.; Héroguel, F.; Steier, L.; Ahmad, S.; Luterbacher, J. S.; Mayer, M. T.; Luo, J.; Grätzel, M. Solar conversion of CO_2 to CO using Earth-abundant electrocatalysts prepared by atomic layer modification of CuO. *Nat. Energy* **2017**, *2*, 17087.
(13) Qing, G.; Hamann, T. W. New Electrolytic Devices Produce Ammonia with Exceptional Selectivity. *Joule* **2019**, *3*, 634−636.
(14) Montoya, J. H.; Tsai, C.; Vojvodic, A.; Nørskov, J. K. The challenge of electrochemical ammonia synthesis: A new perspective on the role of nitrogen scaling relations. *ChemSusChem* **2015**, *8*, 2180−2186.
(15) Singh, A. R.; Rohr, B. A.; Schwalbe, J. A.; Cargnello, M.; Chan, K.; Jaramillo, T. F.; Chorkendorff, I.; Nørskov, J. K. Electrochemical Ammonia Synthesis-The Selectivity Challenge. *ACS Catal.* **2017**, *7*, 706−709.
(16) Singh, A. R.; Rohr, B. A.; Statt, M. J.; Schwalbe, J. A.; Cargnello, M.; Nørskov, J. K. Strategies toward selective electrochemical ammonia synthesis. *ACS Catal.* **2019**, *9*, 8316−8324.
(17) Soloveichik, G. Electrochemical synthesis of ammonia as a potential alternative to the Haber-Bosch process. *Nat. Catal.* **2019**, *2*, 377.
(18) Liu, H.; Wei, L.; Liu, F.; Pei, Z.; Shi, J.; Wang, Z.-j.; He, D.; Chen, Y. Homogeneous, Heterogeneous, and Biological Catalysts for Electrochemical N2 Reduction toward NH3 under Ambient Conditions. *ACS Catal.* **2019**, *9*, 5245−5267.
(19) Zhou, F.; Azofra, L. M.; Ali, M.; Kar, M.; Simonov, A. N.; McDonnell-Worth, C.; Sun, C.; Zhang, X.; MacFarlane, D. R. Electro-synthesis of ammonia from nitrogen at ambient temperature and pressure in ionic liquids. *Energy Environ. Sci.* **2017**, *10*, 2516−2520.
(20) Suryanto, B. H. R.; Kang, C. S. M.; Wang, D.; Xiao, C.; Zhou, F.; Azofra, L. M.; Cavallo, L.; Zhang, X.; MacFarlane, D. R. Rational Electrode-Electrolyte Design for Efficient Ammonia Electrosynthesis under Ambient Conditions. *ACS Energy Lett.* **2018**, *3*, 1219−1224.
(21) Nazemi, M.; Panikkanvalappil, S. R.; El-Sayed, M. A. Enhancing the rate of electrochemical nitrogen reduction reaction for ammonia synthesis under ambient conditions using hollow gold nanocages. *Nano Energy* **2018**, *49*, 316−323.
(22) Nazemi, M.; El-Sayed, M. A. Electrochemical Synthesis of Ammonia from N2 and H2O under Ambient Conditions Using Pore-Size-Controlled Hollow Gold Nanocatalysts with Tunable Plasmonic Properties. *J. Phys. Chem. Lett.* **2018**, *9*, 5160−5166.
(23) Nazemi, M.; Soule, L.; Liu, M.; El-Sayed, M. A. Ambient Ammonia Electrosynthesis from Nitrogen and Water by Incorporating Palladium in Bimetallic Gold-Silver Nanocages. *J. Electrochem. Soc.* **2020**, *167*, 054511.
(24) Zheng, J.; Lyu, Y.; Qiao, M.; Wang, R.; Zhou, Y.; Li, H.; Chen, C.; Li, Y.; Zhou, H.; Jiang, S. P. Photoelectrochemical synthesis of ammonia on the aerophilic-hydrophilic heterostructure with 37.8% efficiency. *Chem* **2019**, *5*, 617−633.
(25) Xue, Z.-H.; Zhang, S.-N.; Lin, Y.-X.; Su, H.; Zhai, G.-Y.; Han, J.-T.; Yu, Q.-Y.; Li, X.-H.; Antonietti, M.; Chen, J.-S. Electrochemical reduction of N_2 into NH_3 by donor−acceptor couples of Ni and Au nanoparticles with a 67.8% Faradaic efficiency. *J. Am. Chem. Soc.* **2019**, *141*, 14976−14980.
(26) Bao, D.; Zhang, Q.; Meng, F.-L.; Zhong, H.-X.; Shi, M.-M.; Zhang, Y.; Yan, J.-M.; Jiang, Q.; Zhang, X.-B. Electrochemical Reduction of N_2 under Ambient Conditions for Artificial N_2 Fixation and Renewable Energy Storage Using N_2/NH_3 Cycle. *Adv. Mater.* **2017**, *29*, 1604799.
(27) Shi, M.-M.; Bao, D.; Wulan, B.-R.; Li, Y.-H.; Zhang, Y.-F.; Yan, J.-M.; Jiang, Q. Au Sub-Nanoclusters on TiO2toward Highly Efficient and Selective Electrocatalyst for N2Conversion to NH3at Ambient Conditions. *Adv. Mater.* **2017**, *29*, 1606550.
(28) Yan, Z.; Ji, M.; Xia, J.; Zhu, H. Recent Advanced Materials for Electrochemical and Photoelectrochemical Synthesis of Ammonia from Dinitrogen: One Step Closer to a Sustainable Energy Future. *Adv. Energy Mater.* **2020**, *10*, 1902020.
(29) Lazouski, N.; Schiffer, Z. J.; Williams, K.; Manthiram, K. Understanding continuous lithium-mediated electrochemical nitrogen reduction. *Joule* **2019**, *3*, 1127−1139.
(30) Lee, H. K.; Koh, C. S. L.; Lee, Y. H.; Liu, C.; Phang, I. Y.; Han, X.; Tsung, C.-K.; Ling, X. Y. Favoring the unfavored: Selective electrochemical nitrogen fixation using a reticular chemistry approach. *Sci. Adv.* **2018**, *4*, No. eaar3208.
(31) Lazouski, N.; Chung, M.; Williams, K.; Gala, M. L.; Manthiram, K. Non-aqueous gas diffusion electrodes for rapid ammonia synthesis from nitrogen and water-splitting-derived hydrogen. *Nat. Catal.* **2020**, *3*, 463−469.
(32) Yang, X.; Nash, J.; Anibal, J.; Dunwell, M.; Kattel, S.; Stavitski, E.; Attenkofer, K.; Chen, J. G.; Yan, Y.; Xu, B. Mechanistic insights into electrochemical nitrogen reduction reaction on vanadium nitride nanoparticles. *J. Am. Chem. Soc.* **2018**, *140*, 13387−13391.
(33) Nash, J.; Yang, X.; Anibal, J.; Wang, J.; Yan, Y.; Xu, B. Electrochemical nitrogen reduction reaction on noble metal catalysts in proton and hydroxide exchange membrane electrolyzers. *J. Electrochem. Soc.* **2017**, *164*, F1712−F1716.
(34) Akagi, F.; Matsuo, T.; Kawaguchi, H. Dinitrogen cleavage by a diniobium tetrahydride complex: formation of a nitride and its conversion into imide species. *Angew. Chem., Int. Ed.* **2007**, *46*, 8778−8781.
(35) Shima, T.; Hu, S.; Luo, G.; Kang, X.; Luo, Y.; Hou, Z. Dinitrogen cleavage and hydrogenation by a trinuclear titanium polyhydride complex. *Science* **2013**, *340*, 1549−1552.
(36) Wang, J.; Yu, L.; Hu, L.; Chen, G.; Xin, H.; Feng, X. Ambient ammonia synthesis via palladium-catalyzed electrohydrogenation of dinitrogen at low overpotential. *Nat. Commun.* **2018**, *9*, 1795.
(37) Suo, L.; Borodin, O.; Gao, T.; Olguin, M.; Ho, J.; Fan, X.; Luo, C.; Wang, C.; Xu, K. "Water-in-salt" electrolyte enables high-voltage aqueous lithium-ion chemistries. *Science* **2015**, *350*, 938−943.
(38) Song, Y.; Johnson, D.; Peng, R.; Hensley, D. K.; Bonnesen, P. V.; Liang, L.; Huang, J.; Yang, F.; Zhang, F.; Qiao, R.; et al. A physical catalyst for the electrolysis of nitrogen to ammonia. *Sci. Adv.* **2018**, *4*, No. e1700336.
(39) Chen, G.-F.; Cao, X.; Wu, S.; Zeng, X.; Ding, L.-X.; Zhu, M.; Wang, H. Ammonia Electrosynthesis with High Selectivity under Ambient Conditions via a Li+ Incorporation Strategy. *J. Am. Chem. Soc.* **2017**, *139*, 9771−9774.
(40) Mahmoud, M. A.; El-Sayed, M. A. Metallic double shell hollow nanocages: the challenges of their synthetic techniques. *Langmuir* **2012**, *28*, 4051−4059.
(41) Valencia, F. J.; González, R. I.; Vega, H.; Ruestes, C.; Rogan, J.; Valdivia, J. A.; Bringa, E. M.; Kiwi, M. Mechanical Properties Obtained by Indentation of Hollow Pd Nanoparticles. *J. Phys. Chem. C* **2018**, *122*, 25035−25042.
(42) Idrissi, H.; Wang, B.; Colla, M. S.; Raskin, J. P.; Schryvers, D.; Pardoen, T. Ultrahigh strain hardening in thin palladium films with nanoscale twins. *Adv. Mater.* **2011**, *23*, 2119−2122.
(43) Higgins, D.; Hahn, C.; Xiang, C.; Jaramillo, T. F.; Weber, A. Z. Gas-diffusion electrodes for carbon dioxide reduction: a new paradigm. *ACS Energy Lett.* **2018**, *4*, 317−324.
(44) Weng, L.-C.; Bell, A. T.; Weber, A. Z. Towards membrane-electrode assembly systems for CO2 reduction: a modeling study. *Energy Environ. Sci.* **2019**, *12*, 1950−1968.
(45) Larrazábal, G. O.; Strøm-Hansen, P.; Heli, J. P.; Zeiter, K.; Therkildsen, K. T.; Chorkendorff, I.; Seger, B. Analysis of Mass Flows and Membrane Cross-over in CO2 Reduction at High Current Densities in an MEA-Type Electrolyzer. *ACS Appl. Mater. Interfaces* **2019**, *11*, 41281−41288.
(46) Nazemi, M.; Padgett, J.; Hatzell, M. C. Acid/base multi-ion exchange membrane-based electrolysis system for water splitting. *Energy Technol.* **2017**, *5*, 1191−1194.
(47) Schmidt, T.; Gasteiger, H.; Stäb, G.; Urban, P.; Kolb, D.; Behm, R. Characterization of high-surface-area electrocatalysts using a rotating disk electrode configuration. *J. Electrochem. Soc.* **2019**, *145*, 2354−2358.
(48) Andersen, S. Z.; Čolić, V.; Yang, S.; Schwalbe, J. A.; Nielander, A. C.; McEnaney, J. M.; Enemark-Rasmussen, K.; Baker, J. G.; Singh, A. R.; Rohr, B. A.; et al. A rigorous electrochemical ammonia synthesis

https://dx.doi.org/10.1021/acscatal.0c02680
ACS Catal. 2020, 10, 10197−10206

protocol with quantitative isotope measurements. *Nature* **2019**, *570*, 504.
(49) Suryanto, B. H. R.; Du, H.-L.; Wang, D.; Chen, J.; Simonov, A. N.; MacFarlane, D. R. Challenges and prospects in the catalysis of electroreduction of nitrogen to ammonia. *Nat. Catal.* **2019**, *2*, 290.
(50) Greenlee, L. F.; Renner, J. N.; Foster, S. L. The use of controls for consistent and accurate measurements of electrocatalytic ammonia synthesis from dinitrogen. *ACS Catal.* **2018**, *8*, 7820.
(51) Nazemi, M.; El-Sayed, M. A. Plasmon-enhanced photo-(electro)chemical nitrogen fixation under ambient conditions using visible light responsive hybrid hollow Au-Ag2O nanocages. *Nano Energy* **2019**, *63*, 103886.
(52) Yao, Y.; Zhu, S.; Wang, H.; Li, H.; Shao, M. A spectroscopic study on the nitrogen electrochemical reduction reaction on gold and platinum surfaces. *J. Am. Chem. Soc.* **2018**, *140*, 1496−1501.
(53) Li, C.; Wang, T.; Zhao, Z.-J.; Yang, W.; Li, J.-F.; Li, A.; Yang, Z.; Ozin, G. A.; Gong, J. Promoted Fixation of Molecular Nitrogen with Surface Oxygen Vacancies on Plasmon-Enhanced TiO2 Photoelectrodes. *Angew. Chem., Int. Ed.* **2018**, *57*, 5278−5282.
(54) Fortes, A. D.; Wood, I. G.; Alfè, D.; Hernández, E. R.; Gutmann, M. J.; Sparkes, H. A. Structure, hydrogen bonding and thermal expansion of ammonium carbonate monohydrate. *Acta Crystallogr., Sect. B: Struct. Sci., Cryst. Eng. Mater.* **2014**, *70*, 948−962.
(55) Wang, H.; Li, Y.; Li, C.; Deng, K.; Wang, Z.; Xu, Y.; Li, X.; Xue, H.; Wang, L. One-pot synthesis of bi-metallic PdRu tripods as an efficient catalyst for electrocatalytic nitrogen reduction to ammonia. *J. Mater. Chem. A* **2019**, *7*, 801−805.
(56) Pang, F.; Wang, Z.; Zhang, K.; He, J.; Zhang, W.; Guo, C.; Ding, Y. Bimodal nanoporous Pd3Cu1 alloy with restrained hydrogen evolution for stable and high yield electrochemical nitrogen reduction. *Nano Energy* **2019**, *58*, 834−841.

https://dx.doi.org/10.1021/acscatal.0c02680
ACS Catal. 2020, 10, 10197−10206